Effect of constraint on cyclic plastic behaviours of cracked bodies and the establishment of unified constraint correlation

Xiaoxiao WANG [1], Jie YANG [2]*, Haofeng CHEN [1,3]*, Zhiyuan MA [1], Fuzhen XUAN [3]

[1] Department of Mechanical & Aerospace Engineering, University of Strathclyde, Glasgow, G1 1XJ, UK

[2] Shanghai Key Laboratory of Multiphase Flow and Heat Transfer in Power Engineering, School of Energy and Power Engineering, University of Shanghai for Science and Technology, Shanghai 200093, PR China

[3] School of Mechanical and Power Engineering, East China University of Science and Technology, Shanghai, 200237, PR China

Abstract: Constraint effect existing in the cracked structures plays a vital role in monotonic loading conditions and affects the material fracture behaviour, it is not clear whether the constraint affects the cyclic plastic responses in the cyclic loading condition. In this research, the laboratory compact tension (CT) and central-cracked tension (CCT) specimens with different in-plane and out-of-plane constraints were selected to explore the constraint effect on the ratchet limit and cyclic plastic behaviour numerically by the liner matching method (LMM). The results show that the plastic shakedown load domain and low cycle fatigue (LCF) life are compressed dramatically by increasing the in-plane constraint effect, while the out-of-plane constraint effect elevates the capability to resist ratcheting failure. In addition, the ratcheting boundary of the cracked specimen is much more sensitive and vulnerable under the influence of the high in-plane constraint effect. Moreover, the unified constraint parameter A_p is suitable to measure the strength of compound constraint under cyclic loading conditions, and there is a salient linear relation between constraint parameter $\sqrt{A_p}$ and cyclic plastic responses (including ratchet limit and alternating plastic strain range) of the cracked specimen. This correlation is very meaningful for evaluating the ratchet limit and low cycle fatigue (LCF) life of cracked structures in terms of different levels of constraint conditions (including different in-plane, out-of-plane, and compound constraint conditions), where the constraint effect is calibrated based on the unified constraint parameter A_p.

Keywords: constraint, cyclic plastic behaviour, unified correlation, cracked body, LMM

---

* Corresponding author. Tel.: +44 141 5482036; fax: +44 141 5525105.

E-mail address: yangjie@usst.edu.cn (J. Yang); haofeng.chen@strath.ac.uk (H. Chen)

Nomenclature

Abbreviations

BCs	boundary conditions
CT	compact tension
CCT	central-cracked tension
DSCA	direct steady cyclic analysis
EPP	elastic-perfectly plastic
FEA	finite element analysis
LCF	low cycle fatigue
LMM	Linear Matching Method
PEMAG	plastic strain magnitude
3D	three-dimensional

Variables

A_{PEEQ}	area surrounded by equivalent alternative plastic strain isoline
A_p	unified parameter for quantifying both in-plane and out-of-plane constraints
A_{ref}	area surrounded by equivalent alternative plastic strain isoline in a standard test
E	Young's modulus
F	cyclic time-dependent surface load
$\bar{F}$	constant component of surface load
I	strain energy function
P	cyclic component of surface load
R^2	correlation coefficient
S_T	surface subjected to surface load
S_u	surface subjected to displacement constraint
V	body volume
W	width parameter of CT and CCT specimens
M_{max}	peak value of the bending moment within the load cycle
a	initial crack length
t	time during the varying load history
ν	Poisson's ratio
Δt	time increment during the load history
λ	a load parameter
$\hat{\sigma}_{ij}$	linear elastic stress corresponding to the time-dependent load condition
$\hat{\sigma}_{ij}^{\bar{F}}$	constant elastic stresses
$\hat{\sigma}_{ij}^{\Delta}$	time-dependent elastic stresses
σ_{ij}	stress solution of the general cyclic load condition
σ_{ij}^{c}	stress at yield state to derive the Minimum Theorem
σ_{ij}^{*}	stress state under yield condition
σ_y	yield stress to derive the ratchet limit
σ_s	material yield strength under room temperature
σ_0	subsequent yield strength in DSCA iteration
$\bar{\rho}_{ij}$	constant residual stress

ρ_{ij}^{r}	time-dependent residual stress
ρ_{kk}^{nf}	hydrostatic component of residual stress under equilibrium condition
$\Delta\rho_{ij}^{nf'}$	deviatoric component of residual stress under equilibrium conditon
$\dot{\varepsilon}_{ij}^{p}$	plastic strain rate
$\dot{\varepsilon}_{ij}^{c}$	kinematically admissible strain rate
$\dot{\varepsilon}_{ij}^{s}$	exact stress solution
$\varepsilon_{ratcheting}$	equivalent ratcheting strain
ε^{pl}	plastic strain tensor
$\Delta\varepsilon_{ij}^{n}$	increment of plastic strain in terms of time t_n
$\Delta\varepsilon_{ij}^{ni}$	initial estimation of $\Delta\varepsilon_{ij}^{n}$
$\Delta\varepsilon_{ij}^{Tf'}$	deviatoric component of compatible strain increment
$\Delta\varepsilon_{ij}^{nf'}$	deviatoric component of plastic strain increment
$\Delta\varepsilon_{kk}^{Tf}$	hydrostatic component of compatible strain increment
f	yield condition function
$\dot{\alpha}$	a plastic multiplier
$\bar{\mu}_{ni}$	shear modulus

1. Introduction

Constraint is the resistance of a structure against plastic deformation [1], which is closely related to the specimen dimension and can be segregated into in-plane constraint and out-of-plane constraint based on the crack plane. The specimen dimensions in the direction of the growing crack, including the crack depth and specimen width, directly affect the in-plane constraint. The specimen dimension parallels the crack front, which includes specimen thickness, directly determining the out-of-plane constraint.

Given that constraint can significantly affect the material fracture resistance, it is essential to understand its effect on material fracture behaviour clearly. Therefore, a lot of studies have been done on the effect of constraint on the material fracture behaviour under monotonic loading, and different fracture constraint parameters and theories, such as K-T [2], J-Q [3, 4], J-A_2 [5], T_Z [6-8], φ [9-12], A_p [13-15], and A_d [16] have been developed to characterise and analyse the constraint effect. In addition, to deal with the high-temperature structural integrity assessment falling into the creep regime, the constraint parameters Q^* [17] and C^*-Q^* [18] were proposed, with the recent findings of the constraint effect on creep crack initiation reported in Ref. [19].

In addition, as an important factor that affects the stress and strain fields at the crack tip, constraint not only exists in the structures and affects the material fracture behaviour under monotonic loading mentioned above, but also changes the cyclic plastic response of cracked structures (including ratcheting and low cycle fatigue (LCF)) under cyclic loading. Ratcheting failure is one of the three typical cyclic states (elastic shakedown, plastic shakedown and ratcheting) of material and engineering structure under cyclic loading when load condition is outside the plastic shakedown region, which ultimately leads to intolerable progressive plastic deformations and significantly reduces the residual life of the material and engineering structure. Another structural response concerning cyclic load conditions is

the plastic shakedown or alternating plasticity, with the load condition lying lower than the ratcheting boundary. Under the alternating plasticity state, the LCF damage accumulates gradually in the local region, finally leading to the fatigue crack initiation in terms of the local plastic strain amplitude [20]. Since the elastic stress singularity at the crack tip makes the elastic shakedown condition invalid and meaningless, the finite elastic shakedown limit does not exist anymore [21, 22]. On the contrary, the procedures for identifying the ratchet limit and alternating plasticity are still valid due to the closed cycles of plastic strains occurring at the crack tip, enabling the evaluation of the finite ratchet limits. Thus, it is significant to investigate the cyclic plastic response of the material and cracked engineering structure considering the constraint effect.

Due to the high sensitivity of the crack tip to the cyclic structural responses [23], enormous properly refined elements should be involved during discretizing of the cracked components, especially for the crack tip location [24] where the gradients of stress and strain are susceptible to the crack size. Hence, given the better balance between computational accuracy and efficiency, several numerical procedures were developed and devoted to addressing the ratcheting of a material or engineering structure with a crack. Chen et al. [21, 22] proposed the Linear Matching Method (LMM) and applied it to study the effect of circular holes on the ratchet limit in a centre-cracked plate. Li et al. [25] analysed the ratchet limit of a pipe with an axisymmetric circumferential crack in a mismatched weld. Tong et al. [26] predicted the crack growth rate in a vacuum environment by including both ratcheting strain and accumulated inelastic strain near the crack tip. In addition to these main factors affecting the ratchet limit including cyclic load type, load level, crack location and size, the majority of current understanding attributed the influence of the crack on the ratcheting behaviour to the local highly discontinuous geometric effects and the related examinations mainly concentrated on the distribution rules and shape of the cyclic plastic zone [27, 28].

To reasonably address the structural integrity assessment containing defects, it is crucial to deal with the constraint effect in the detailed calculations of structural response, and hence, the engineering standards [29-32] have incorporated the constraint effect into the analysis procedures. Several numerical investigations of the constraint effect on fatigue crack evaluation were reported by Refs. [33-35], which defined and utilized the constraint parameters to describe the underlying influence of the constraint effect on the predictions of crack propagation life. Furthermore, the studies of constraint effect matching between the laboratory standard specimens and actual engineering components were explored, with specified applications to the steam turbine blade [36] and cracked pipeline [37] elaborated under monotonic load conditions.

However, the effect of constraint on the ratchet limit and alternating plasticity in different cracked specimens has not been studied clearly. And so far, there is no evidence to show whether there is a certain correlation between the constraint effect and the cyclic plastic response or whether there is a suitable constraint parameter that is able to characterise the influence of the constraint effect on the cyclic plastic response.

In this research, the first motivation is to investigate the effect of constraint conditions on the cyclic responses of cracked structures, including the reverse plasticity and ratcheting behaviour. And this analysis is aiming at establishing ratcheting boundaries for the cracked specimens as well as revealing the influence mechanisms of different constraint conditions. And the second purpose is to find an appropriate constraint effect parameter which has the capability to clearly depict the relationship between the ratchet limit and the strength of constraint and the relationship between the cyclic plastic strain range and the strength of constraint in terms of the cracked specimen. It is also intended to explore the potential of such a relationship in assessing cracked engineering structures. Last but not least, the third aim is to verify all the numerical processes which are applied in the virtual experiments when deriving the pertinent constraint parameter.

The structure of this manuscript is outlined as follows:

In Section 2, the numerical method, LMM procedures, to deal with the cyclic plastic responses is elaborated. Then, the selected experimental specimens, the laboratory compact tension (CT) and central-cracked tension (CCT) specimens with different in-plane and out-of-plane constraint conditions, are described in Section 3. And in Section 4, the interactive boundaries of ratcheting and constraint effect are constructed, with the mechanisms of the constraint effect on the ratchet limit and alternating plastic strain range in different cracked specimens analyzed comprehensively. Furthermore, the unified constraint parameter A_p is employed to reflect the strength of both in-plane and out-of-plane constraint conditions during ratcheting and alternating plasticity analyses. And the linear correlation between the parameter $\sqrt{A_p}$ and the cyclic plastic response of the cracked specimen is also derived. Next, a series of numerical verifications are presented in Section 5, where the effectiveness and accuracy of the proposed analysis strategy are demonstrated in detail. In the last section, the main conclusions of this study are summarized.

2. Numerical procedures

2.1. Definition of cyclic load history

When an elastic-perfectly plastic (EPP) made structure is subjected to a general cyclic load, this condition can be decoupled into cyclic and constant components. It can be assumed that a structure is subjected to a cyclic time-dependent surface load $F(x_i, t)$ applied on the part of the structure surface S_T. On the rest surface S_u, the displacement rate should be equal to zero. The process is considered over a full cycle from $t = 0$ to $t = \Delta t$. After decomposing the cyclic load condition into a cyclic and constant part [38], it can be represented by the following load:

$$F(x_i,t) = \lambda \bar{F}(x_i) + P(x_i,t) \tag{1}$$

here λ is a load parameter, $\bar{F}(x_i)$ is the constant load component and $P(x_i,t)$ is the cyclic part. The linear elastic stress corresponding to the time-dependent load condition is calculated by Equation (2):

$$\hat{\sigma}_{ij}(x_k,t) = \lambda \hat{\sigma}_{ij}^{\bar{F}} + \hat{\sigma}_{ij}^{\Delta}(x_k,t) \tag{2}$$

Here it can be seen that by changing the load parameter λ, the whole process during a full cycle can be taken into account.

2.2. Asymptotic cyclic solution

There are three components inside one typical response cycle: the elastic response which is a transient response accumulated up to the beginning of the cycle, and a residual component making contributes to the remaining change in the cycle [39]. The stress solution of the general cyclic load condition is comprised of the time-dependent and constant residual stress component, which is expressed by Equation (3):

$$\sigma_{ij}(x_k,t) = \hat{\sigma}_{ij}(x_k,t) + \bar{\rho}_{ij}(x_k) + \rho_{ij}^{r}(x_k,t) \tag{3}$$

where $\hat{\sigma}_{ij}$ is the elastic component, and $\bar{\rho}_{ij}$ is a constant stress field on equilibrium with a zero surface boundary condition state, corresponding to the residual stress field at the start and end of the cycle. And the time-dependent residual component over the cycle meet the condition:

$$\rho_{ij}^{r}(x_k,0) = \rho_{ij}^{r}(x_k,\Delta t) = 0 \tag{4}$$

2.3. Minimum Theorem in Excess of Shakedown

The plastic strain is defined by a convex yield condition:

$$f(\sigma_{ij}) \leq 0 \tag{5}$$

and the associated flow law is:

$$\dot{\varepsilon}_{ij}^{p} = \dot{\alpha}\frac{\partial f}{\partial \sigma_{ij}}, \qquad f = 0 \tag{6}$$

where $\dot{\alpha}$ is a plastic multiplier, and the maximum work principle should be:

$$(\sigma_{ij}^{c} - \sigma_{ij}^{*})\dot{\varepsilon}_{ij}^{c} \geq 0 \tag{7}$$

where σ_{ij}^{c} is the stress at yield state, $f(\sigma_{ij}^{c}) = 0$, associated with the flow law above, with the plastic strain rate $\dot{\varepsilon}_{ij}^{p} = \dot{\varepsilon}_{ij}^{c}$. And σ_{ij}^{*} represents any stress state that meets the yield condition, $f(\sigma_{ij}^{*}) \leq 0$.

Here a strain energy function [21] is defined as

$$I(\dot{\varepsilon}_{ij}^{c}, \lambda) = \int_{V}\int_{0}^{\Delta t}\left(\sigma_{ij}^{c} - \lambda\hat{\sigma}_{ij}^{\bar{F}} - \hat{\sigma}_{ij}^{\Delta}(x_k, t)\right)\dot{\varepsilon}_{ij}^{c}dtdV \tag{8}$$

where $\dot{\varepsilon}_{ij}^{c}$ is the kinematically admissible strain rate.

There also exists a load parameter so that

$$f\left(\lambda\hat{\sigma}_{ij}^{\bar{F}} + \hat{\sigma}_{ij}^{\Delta}(x_k, t) + \bar{\rho}_{ij}(x_k) + \rho_{ij}^{r}(x_k, t)\right) \leq 0 \tag{9}$$

and that

$$I(\dot{\varepsilon}_{ij}^{c}, \lambda) \geq I(\dot{\varepsilon}_{ij}^{s}, \lambda) \tag{10}$$

where $\dot{\varepsilon}_{ij}^{s}$ is the exact solution.

2.4. The determinations of time-dependent residual stress field and plastic strain range

The whole numerical strategy contains two processes. Step one is to implement a direct steady cyclic analysis (DSCA) to address the time-dependent residual stress field and the corresponding plastic strain range due to the cyclic load condition. Step two is to calculate

the ratchet limit by performing a general shakedown analysis [40], during which the convergent constant residual stress solution is acquired with the elastic stress solution scaled.

It can be assumed that in a deviatoric stress component space, the plastic strain occurs only at the load vertexes, which corresponds to N time points, $t_1, t_2, \dots, t_N$, in the cyclic load condition, leading to $\Delta\varepsilon_{ij}^{c} = \Sigma_{n=1}^{N}\Delta\varepsilon_{ij}^{n}$. Here $\Delta\varepsilon_{ij}^{n}$ is the increment of plastic strain in terms of time t_n. The strain energy function is approximated by the following equations:

$$I\left(\varepsilon_{ij}^{c}, \lambda\right) = \sum_{n=1}^{N} I^{n} \tag{11}$$

$$I^{n}\left(\Delta\varepsilon_{ij}^{n}, \rho_{ij}(t_n)\right) = \int_{V}\left\{\sigma_{ij}^{n}\Delta\varepsilon_{ij}^{n} - \left(\hat{\sigma}_{ij}^{\Delta}(t_n) + \rho_{ij}(t_n)\right)\Delta\varepsilon_{ij}^{n}\right\}dV \tag{12}$$

where the strain increment is compatible and the residual stress field is equilibrium.

Considering that based on isotropic elastic properties and a von Mises yield condition, the shear modulus $\bar{\mu}_{ni}$ is defined by matching condition linearly,

$$\sigma_y = 2\bar{\mu}_{ni}\bar{\varepsilon}\left(\Delta\varepsilon_{ij}^{ni}\right) \tag{13}$$

where σ_y is the Mises yield stress, and the initial estimation of $\Delta\varepsilon_{ij}^{n}$ is set to be equal to $\Delta\varepsilon_{ij}^{ni}$. The following linear equations can be solved :

$$\Delta\varepsilon_{ij}^{Tf'} = \frac{1}{2\mu}\Delta\rho_{ij}^{nf'} + \Delta\varepsilon_{ij}^{nf'}, \Delta\varepsilon_{kk}^{Tf} = \frac{1}{3K}\Delta\rho_{kk}^{nf} \tag{14}$$

$$\Delta\varepsilon_{ij}^{nf'} = \frac{1}{2\bar{\mu}_{ni}}\left\{\hat{\sigma}_{ij}^{\Delta}(t_n) + \rho_{ij}(t_{n-1}) + \Delta\rho_{ij}^{nf}\right\}' \tag{15}$$

where

$$\rho_{ij}(t_{n-1}) = \rho_{ij}(t_0) + \Delta\rho_{ij}^{1} + \Delta\rho_{ij}^{2} + \cdots + \Delta\rho_{ij}^{n-1}, \qquad \rho_{ij}(t_0) = \bar{\rho}_{ij} \tag{16}$$

It should be noted that the mark $'$ means the deviatoric component, and the subscript kk represents the hydrostatic component.

An efficient numerical strategy is proposed to address the linear equations. At the first load point t_1, the iteration is to calculate the time-dependent residual stress field $\Delta\rho_{ij}^{1}$

corresponding to the elastic solution $\hat{\sigma}_{ij}^{\Delta}(t_1)$. $\Delta\rho_{ij_m}^{n}$ is considered as the time-dependent residual stress field for the nth load point during mth cycle, where $n = 1,2,\dots,N$ and $m = 1,2,\dots,M$. The time-dependent residual stress field for all load points at each cycle should be computed, and after satisfying the convergence, the sum of every time-dependent residual stress field at each load point should be equal to zero. At the same time, the constant residual stress field can be derived by

$$\bar{\rho}_{ij} = \sum_{n=1}^{N} \Delta\rho_{ij_1}^{n} + \sum_{n=1}^{N} \Delta\rho_{ij_2}^{n} + \cdots + \sum_{n=1}^{N} \Delta\rho_{ij_M}^{n} \tag{17}$$

Accordingly, the plastic strain amplitude for the load point n is evaluated by

$$\Delta\varepsilon_{ij}^{P}(t_n) = \frac{1}{2\bar{\mu}_n}\left(\hat{\sigma}_{ij}^{\Delta'}(t_n) + \rho_{ij}'(t_n)\right) \tag{18}$$

Then, at the end of each iteration, the subsequent yield strength $\sigma_0^m(t_n)$ at the load instance t_n associated with the current plastic strain is re-calculated if needed when the strain hardening model is involved in the material property. And the linear matching condition is able to be updated at the last step of each iteration process by

$$\bar{\mu}_{m+1}(t_n) = \bar{\mu}_m(t_n)\frac{\sigma_0^m(t_n)}{\bar{\sigma}\left(\hat{\sigma}_{ij}^{\Delta}(t_n) + \rho_{ij}^{m}(t_n)\right)} \tag{19}$$

The detailed numerical procedure of the Direct Steady Cycle Analysis (DSCA) is provided in Fig. 1, where the cyclic plastic response is given out iteratively.

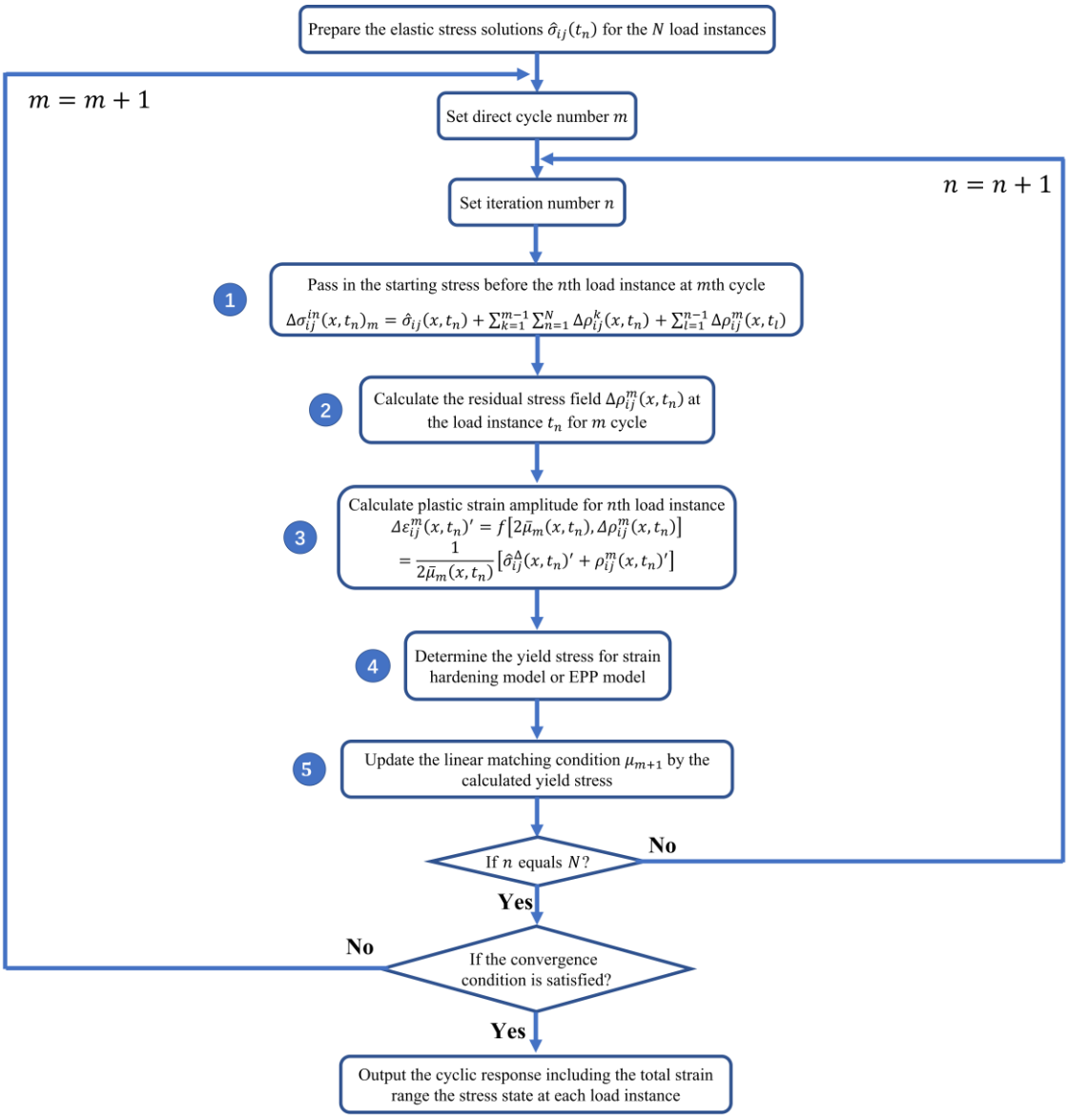

Fig. 1. Detailed iteration process of the DSCA procedure for cyclic plastic response calculation

2.5. Numerical procedure for ratchet limit calculation under the LMM framework

Under the LMM framework, the numerical procedure to calculate the ratchet limit contains two stages. In the first stage, the time-dependent residual stress related to the cyclic component of the load condition is acquired [38] by the proposed DSCA procedure as shown in section 2.4, where the LCF life is able to be evaluated by means of the obtained cyclic

strain range. Then, in the second stage, the ratchet limit can be addressed by the established shakedown analysis procedure [40] based on the upper bound shakedown theory in Equation (20), with the augmented elastic stress field by the changing residual stress history calculated in the first stage.

$$\int_0^{\Delta t}\int_V \hat{\sigma}_{ij}\varepsilon_{ij}^c dtdV = \int_0^{\Delta t}\int_V \sigma_{ij}^c\varepsilon_{ij}^c dtdV \tag{20}$$

$$\hat{\sigma}_{ij} = \lambda\hat{\sigma}_{ij}^{\bar{F}} + \hat{\sigma}_{ij}^{\Delta}(x_k,t) + \rho_{ij}(x_k,t) \tag{21}$$

Given the von Mises yield condition and the associated flow rule, the strain energy associated with the yield state can be rewritten by

$$\int_0^{\Delta t}\int_V \sigma_{ij}^c\varepsilon_{ij}^c dtdV = \int_V^N \sum_{n=1}^{N} \sigma_{ij}^{c^n}\Delta\varepsilon_{ij}^n dV = \int_V \sum_{n=1}^{N} \sigma_y\bar{\varepsilon}\left(\Delta\varepsilon_{ij}^n\right)dV \tag{22}$$

where

$$\bar{\varepsilon}\left(\Delta\varepsilon_{ij}^n\right) = \sqrt{\frac{2}{3}\Delta\varepsilon_{ij}^n\Delta\varepsilon_{ij}^n} \tag{23}$$

Finally, the upper bound ratchet limit multiplier is expressed iteratively by a series of monotonically reducing upper bound ratcheting multipliers, defined by Equation (24), to predict the converged structural ratchet limit,

$$\lambda = \frac{\int_V \sum_{n=1}^{N} \sigma_y\bar{\varepsilon}\left(\Delta\varepsilon_{ij}^n\right)dV - \int_V \sum_{n=1}^{N}\left(\hat{\sigma}_{ij}^{\Delta}(t_n) + \rho_{ij}(t_n)\right)\Delta\varepsilon_{ij}^n dV}{\int_V \hat{\sigma}_{ij}^{\bar{F}}\left(\sum_{n=1}^{N}\Delta\varepsilon_{ij}^n\right)dV} \tag{24}$$

and the physical meaning of this load multiplier is the maximum capacity of the structure with a predefined cyclic load condition to withstand an additional constant load before ratcheting.

3. CT and CCT specimens with different constraint conditions

In this section, the virtual compact tension (CT) specimen and central-cracked tension (CCT) specimen are selected as the numerical models to investigate the influence of the constraint effect on the structural cyclic responses including the alternating plasticity and the ratcheting. The flowchart below displays the whole analysis procedure and application plan of the numerical strategies illustrated above.

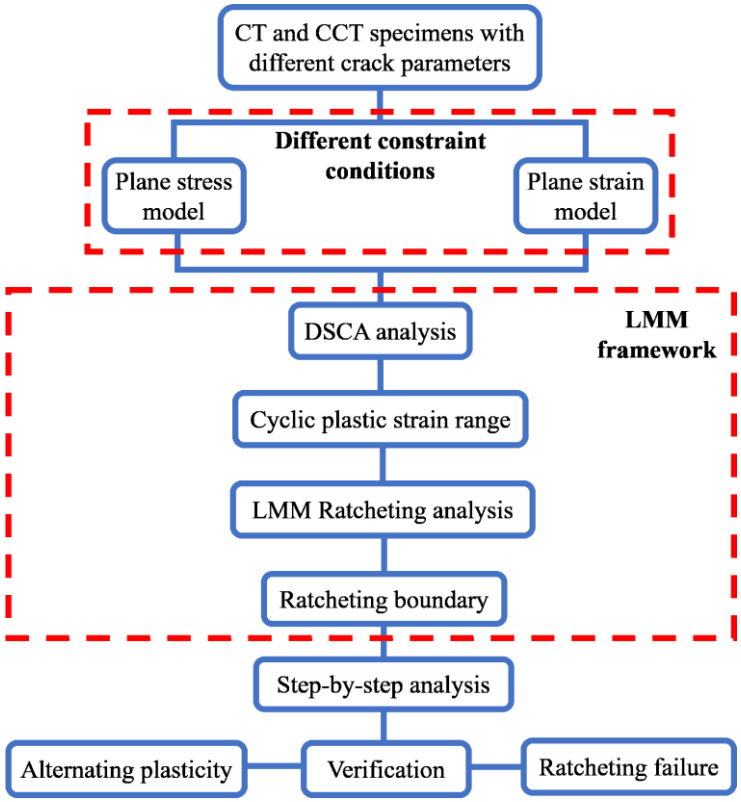

Fig. 2. Analysis strategy and application of the LMM DSCA and ratcheting analyses

3.1. The design of CT and CCT specimens

Two sets of specimens containing compact tension (CT) specimen and central-cracked tension (CCT) specimen, with different loading configurations and geometrical features, are used in the subsequent finite element analysis (FEA), displayed in Fig. 3. To examine the in-plane constraint effect, four series of crack depths ratios denoted as $a/W = 0.1$, 0.3, 0.5 and 0.7 ($W = 32mm$) are set for the CT and CCT specimens, reflecting the intensity of the

constraint conditions, from low to high. On the other hand, plane stress and plane strain 2D conditions are employed respectively to distinguish the difference between out-of-plane constraint effects [41, 42], where the plane strain model provides the highest out-of-plane constraint condition for the cracked specimen, compared to the plane stress model with the lowest out-of-plane constraint condition.

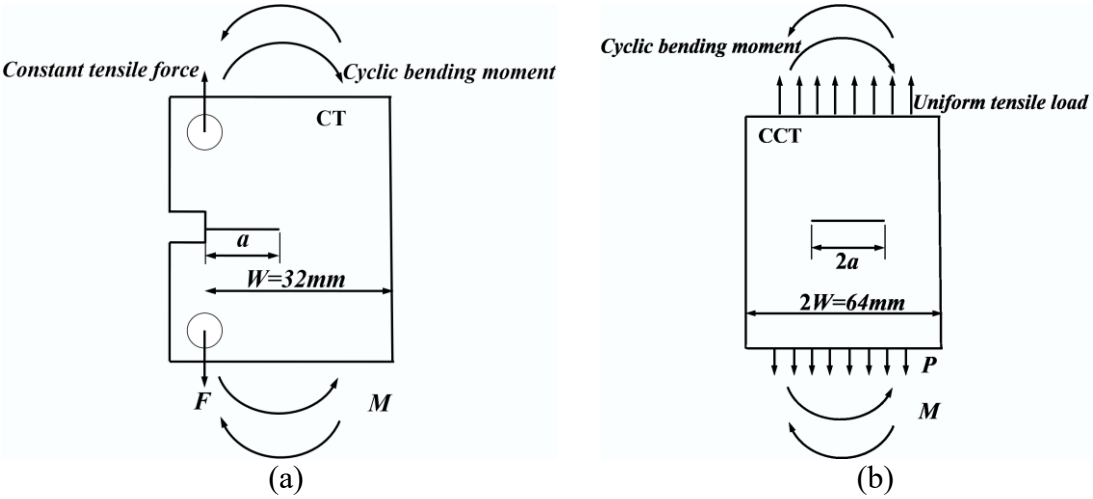

Fig. 3. Loading configurations and geometries of the (a) CT specimen and (b) CCT specimen

3.2. Descriptions of material property and FEA models

Both types of specimens are made of low alloy steel SA508 CL.3 which is widely used for pressure vessels in nuclear engineering [43, 44]. The cyclic behaviour of the material is described by the Ramberg-Osgood (R-O) model to provide the stress-strain relationship for the following FE analysis [45], and the cyclic response is approximated as follows,

$$\varepsilon_{ta} = \frac{\sigma_a}{\bar{E}} + \left(\frac{\sigma_a}{K}\right)^{\frac{1}{n}} \tag{25}$$

$$\bar{E} = \frac{3E}{2(1+v)} \tag{26}$$

where ε_{ta} is the total true strain amplitude, σ_a is the total stress amplitude, $\bar{E}$ is the multi-axial Young's modulus, $K = 660$ and $n = 0.116$ are the material parameters for the cyclic stress-strain curve model under room temperature, $E = 200GPa$ is the modulus of elasticity [44, 46, 47], and the Poisson's ratio v is defined to be 0.3.

Since the 2D model can completely describe the in-plane constraint effect, and the plane strain and plane stress model are capable of maximising the difference between in-plane and out-of-plane constraint effect, the 8-node quadrilateral plane strain and plane stress elements with reduced integration CPE8R and CPS8R [48] respectively are adopted to discretise the CT and CCT specimens in ABAQUS. Besides, around the crack tip, to reflect the highly complicated stress and strain fields and the gradients of various physical quantities, a fine mesh configuration having a focused ring of elements surrounding the crack front is used with a small initial root radius (2 μm) at the crack tip (blunt tip) to enhance convergence of the nonlinear iterations, which is shown in Fig. 4 (in the red rectangle).

Due to the symmetry condition of the two types of specimens in the vertical direction, half models are created to save computing resources. For the CT specimen, a constant tensile force is applied on the left loading hole (see Fig. 3 (a)), and the CCT model is subjected to a constant tensile load which is exerted on the top surface (see Fig. 3 (b)). To simulate the effect of the cyclic bending moment history in Fig. 5, an equivalent cyclic linear distribution of stress is applied to the top boundary of each specimen. Unlike the CT specimen which presents 1 symmetry plane, the CCT specimen normally presents 2 symmetry planes. However, the applied cyclic bending moment on the top boundary leads to loading conditions that are not usual in classic CCT specimens, i.e., one loading symmetry is lost. Therefore,

only one symmetric condition is applied on the symmetric plane for both the CT and CCT specimen in the presence of the top bending moment as shown in Fig. 3 (b), and the half model is adopted for the study of both the CT and CCT specimens.

Moreover, both models are well constrained along the vertical direction, and another extra node is constrained in the horizontal direction to prevent rigid body displacement in each case. The spectrums of time-dependent loads in Fig. 5 depict the cyclic modes of bending moment and tensile load, where all the reference loads are set to be one unit firstly, and then gradually scaled to the ratchet limit during the LMM ratcheting analysis.

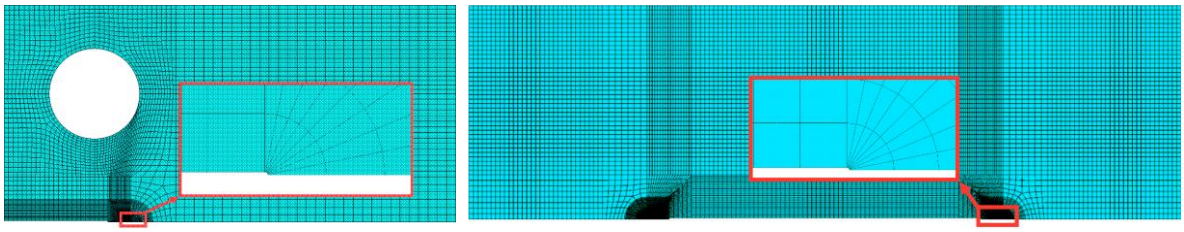

Fig. 4. FEA model and the feature of crack tip: (a) CT specimen and (b) CCT specimen

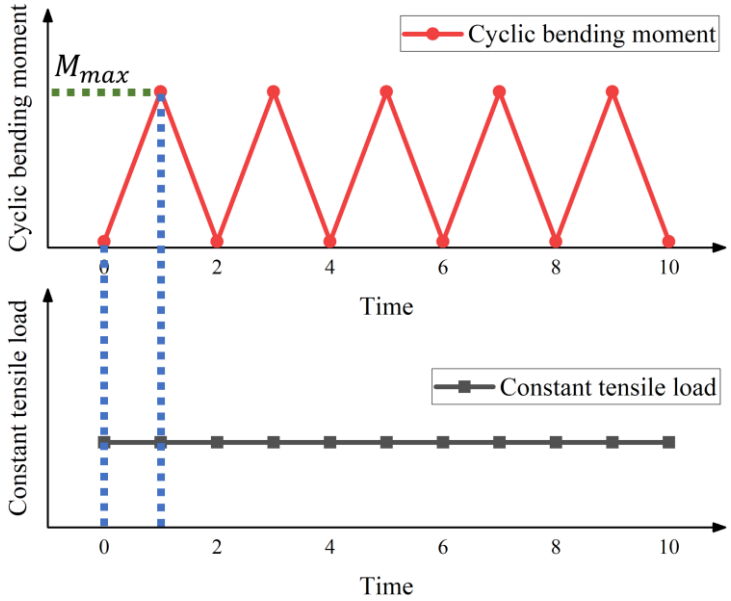

Fig. 5. Load spectrum of cyclic bending moment and constant tensile load

4. Effect of constraint on the ratchet limit and plastic strain range

The ratcheting boundary is capable of distinguishing different types of failure modes, including elastic shakedown, plastic shakedown or alternating plasticity and progressive plasticity or ratcheting behaviour. In this section, by repeatedly adopting the LMM ratcheting analysis at different levels of the cyclic load conditions, a series of ratchet limit boundaries of the provided load combinations are built for the CT and CCT specimens based on the presented LMM DSCA and ratcheting programs.

4.1. Ratcheting boundary of CT specimen with different constraint conditions

In the case of the CT specimen, the ratcheting boundaries under different constraint conditions are calculated by LMM ratcheting analysis considering a sequence of different cyclic bending moment levels, which are described in Fig. 6, where the horizontal and vertical axes represent the constant tensile force applied on the loading hole and the cyclic bending moment, respectively. It can be observed from both plane stress and plane strain CT specimens that, with the increasing in-plane constraint (a/W), the acceptable plastic shakedown region (including elastic and plastic shakedown or alternating plasticity) is compressed inward continuously. That means, resulting from the enhancement of the in-plane constraint effect, the capacity of the structure against cyclic loads is severely weakened, which is similar to the effect of reducing the fracture resistance of the structure.

Traditionally, there should be a linear relationship between the limit load of the structure and the effective cross-section. Conversely, as the dimension of the crack grows linearly, the limit capability of the structure that should have been linearly decreasing shows a highly nonlinear trend. Compared to the results of CT specimens with low constraint ($a/W = 0.1$ and $a/W = 0.3$), the ratcheting boundary shrinks inward more obviously, and the magnitude of change is also more significant in the CT specimens with high constraint ($a/W = 0.5$ and

$a/W = 0.7$), which reflects that the higher constraint effect brings more remarkable change to the ratcheting boundary. In other words, the fluctuation of the ratchet limit is more sensitive under the high constraint effect, and, accordingly, the ratcheting boundary reduces more drastically and nonlinearly, which is caused by the complex response of the ratchet limit to the interaction of the high constraint effect and the reduction of the effective section.

Besides, in terms of out-of-plane constraint effects, by comparing plane stress and plane strain models with the same degree of in-plane constraint condition (a/W) and load conditions, it can be seen that the ratchet limit of the plane strain model is higher than that of the plane stress model. Although the plane strain model corresponds to a higher out-of-plane constraint effect, considering that the ratchet limit is a measure of the overall capacity of the whole structure, the increase in thickness conceals the weakening by the high out-of-plane constraint effect, resulting in the ratchet limit greater than plane stress model.

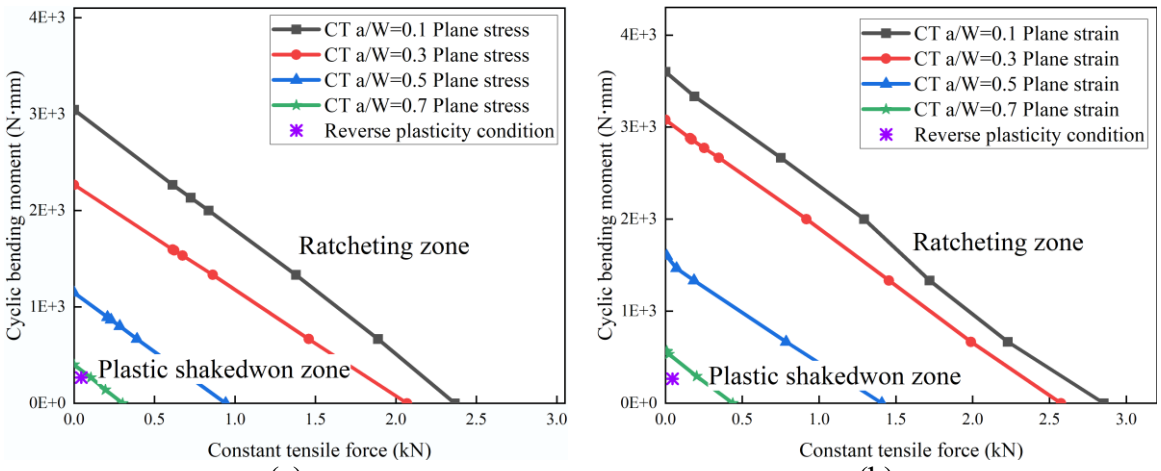

Fig. 6. Ratcheting boundary of CT specimen: with (a) plane stress condition and (b) plane strain condition

4.2. Ratcheting boundary of CCT specimen with different constraint conditions

For the case of the CCT specimen, by employing the same numerical procedure to implement LMM ratcheting analysis, the ratcheting boundaries under different constraint conditions are constructed below in Fig. 7. Compared with the CT specimen mentioned above, a similar phenomenon can be noticed in both plane stress and plane strain models that the acceptable plastic shakedown region under each ratcheting boundary keeps remarkably shrinking as the in-plane constraint increases.

In addition, it is worth pointing out that although when the crack dimension (a/W) is between 0.1 and 0.5, these three ratcheting boundaries (the curves in black, red and blue) have a coincident segment in the interval of elevated cyclic bending moment level (inside the dotted rectangle), the ratcheting boundaries corresponding to crack sizes of 0.3 and 0.5 start to deviate from the ratcheting boundary with the lowest in-plane constraint ($a/W = 0.1$) successively. Forced by a stronger constraint effect in the CCT specimen, when considering the highest in-plane constraint ($a/W = 0.7$), this ratcheting boundary (the curves presented in green) is completely separated from the previous three curves, where the value of reverse plasticity limit due to the cyclic bending moment is much lower than the previous three curves, which finally leads to the minimum plastic shakedown area.

Here it should be clarified that the constraint effect introduced by CCT specimens is weaker than that of CT specimens, hence the ratcheting boundaries of CCT specimens have a specific dense overlap area inside the dotted rectangles highlighted in Fig. 7, leading to a weaker separation of each boundary under the elevated cyclic bending moment level. However, the CT specimen, which symbolises a higher constraint effect, has a clearer degree of separation between each ratcheting boundary shown in Fig. 6. Hence, a general conclusion can be drawn that the ratcheting boundary of the cracked specimen is much more sensitive and vulnerable under the influence of high constraint effects.

Similarly, considering the out-of-plane constraint effect between CCT plane stress and plane strain models, the acceptable plastic shakedown regions (areas under the corresponding

ratcheting boundaries in Fig. 7) of the plane strain model are much broader than that of the plane stress model, where the thickness is dominant in the comparative analysis. In other words, the out-of-plane constraint effect elevates the capability to resist ratcheting failure.

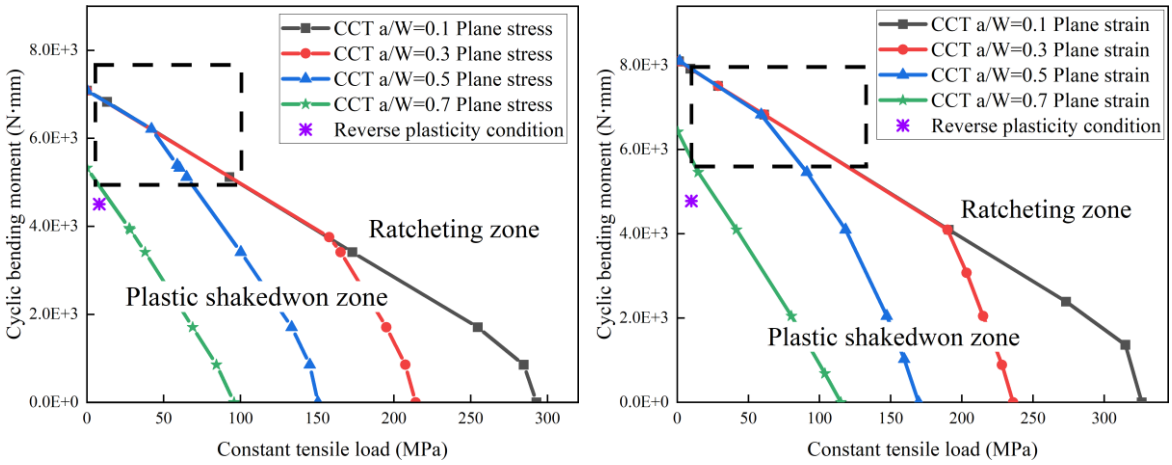

(a) (b)

Fig. 7. Ratcheting boundary of CCT specimen: with (a) plane stress condition and (b) plane strain condition

4.3. Unified correlation between constraint and the ratchet limit

To characterise the in-plane and out-of-plane constraint effect numerically, the unified measure parameter A_p was proposed by Yang et al. [15], which is defined as follows:

$$A_p = A_{PEEQ}/A_{ref} \tag{26}$$

Here, A_{PEEQ} is the area surrounded by the equivalent plastic strain isolines ahead of the crack tip, and A_{ref} is the reference area surrounded by the isolines in the standard specimen, which is selected following the requirement of Ref. [49, 50], with the geometrical feature defined as $a/W = 0.5$.

In this study, the isoline of effective ratcheting strain $\varepsilon_{ratcheting} = 0.2$ ahead of the crack tip is used to calculate the A_{PEEQ}, where the effective ratcheting strain describes the

net increment of the plastic strain after one entire load cycle (including one loading stage and one unloading stage), and A_{ref} is the reference area measured at the ratcheting state in the standard test with a standard CT plane strain model ($a/W = 0.5$).

The areas surrounded by the $\varepsilon_{ratcheting} = 0.2$ isolines are shown in Fig. 8 to Fig. 11 below. For each type of specimen, the ratcheting strain is calculated under the same level of cyclic bend moment, with the constant load located slightly outside the ratcheting boundaries in Fig. 6 and Fig. 7 constructed by LMM analyses. This is intended to avoid the numerical error for which the ratcheting strain is too weak to identify due to the disturbance with the load condition point just located on the ratchet limit boundary, and, consequently, to maintain the fair ratcheting level when demonstrating different constraint conditions.

As crack size a/W increases from 0.1 to 0.7, the in-plane constraint effect strengthens gradually, and, as a result, the areas (in red colour) surrounded by the $\varepsilon_{ratcheting} = 0.2$ isolines show a decreasing trend in both CT and CCT specimens. In addition, by comparing the areas surrounded by the $\varepsilon_{ratcheting} = 0.2$ isolines of plane stress and plane strain model under the same a/W level (e.g., comparing the results in Fig. 8 (a) and Fig. 9 (a)), the results of plane strain models are much lower than those of plane stress models, where the strongest out-of-plane constraint condition of the plane strain model [51] inhibits the development of ratcheting strain at the crack tip during the load combination outside the ratcheting boundary. Here, the plastic strain around the edge of the loading hole is generated by the contact stress between the supporting rollers and the inner surfaces of the loading hole during the movement of the rollers. However, as the loading hole is quite far from the crack tip, the ratcheting strain around the loading hole will not affect ratcheting results at the crack tip. Therefore, there is little impact of the ratcheting strain around the loading hole on the results in the paper. Another noticeable difference is that due to the higher out-of-plane constraint level of plane strain models, relative to plane stress models, the shapes of areas of $\varepsilon_{ratcheting} = 0.2$ isolines

of the plane strain model present a drop shape, which is more concentrated at the crack tip. However, in the plane stress model, the shapes of areas of $\varepsilon_{ratcheting} = 0.2$ isolines present a more widely distributed semi-ellipse.

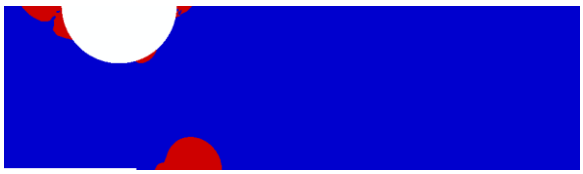

(a) $a/W = 0.1$

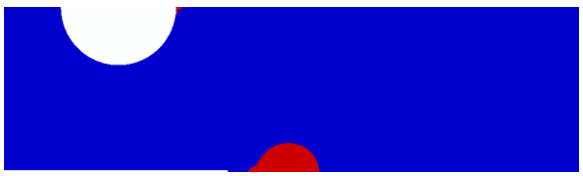

(b) $a/W = 0.3$

(c) $a/W = 0.5$

(d) $a/W = 0.7$

Fig. 8. The ratcheting strain contours of CT plane stress model with different a/W

(a) $a/W = 0.1$

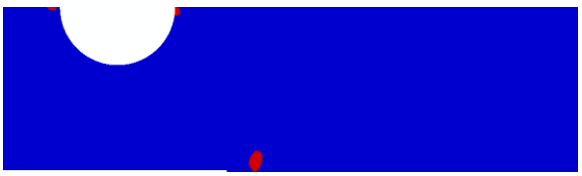

(b) $a/W = 0.3$

(c) $a/W = 0.5$

(c) $a/W = 0.7$

Fig. 9. The ratcheting strain contours of CT plane strain model with different a/W

(a) $a/W = 0.1$

(a) $a/W = 0.1$

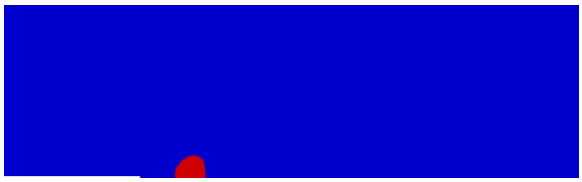

(b) $a/W = 0.3$

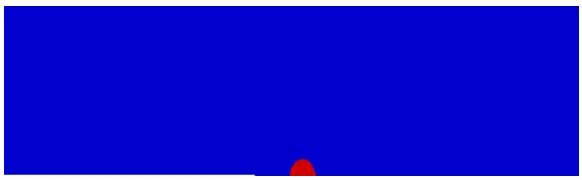

(c) $a/W = 0.5$

(d) $a/W = 0.7$

Fig. 10. The ratcheting strain contours of the CCT plane stress model with different a/W

(b) $a/W = 0.3$

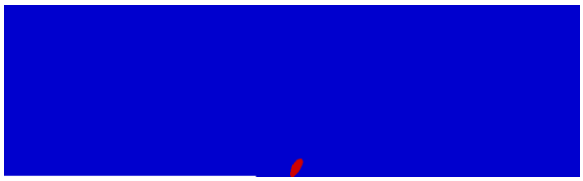

(c) $a/W = 0.5$

(d) $a/W = 0.7$

Fig. 11. The ratcheting strain contours of the CCT plane strain model with different a/W

Fig. 12 shows the unified constraint parameter A_p under different constraint conditions. It can be found that the unified constraint parameter A_p is also suitable for measuring the compound constraint effect of cracked specimens with cyclic loading conditions. Quite similar to the case of monotonic loading condition, as the constraint effect enhances (for the in-plane constraint condition, it refers to the increase of a/W crack dimension, and regarding the out-of-plane constraint condition, it means changing the thickness from plane stress to plane strain), the unified constraint parameter A_p reflects a negative correlation with the constraint condition. At the same time, a lower level of A_p stands for a highly constrained condition, where only limited ratcheting strain develops, while a higher magnitude of A_p indicates a loss of constraint with a much broader ratcheting strain distribution around the crack tip region.

In addition, Fig. 13 further reveals that under the identical predefined level of cyclic bending moment, the ratchet limit of the cracked specimen and the unified constraint parameter $\sqrt{A_p}$ approximately show a salient linear correlation, reflecting the weakness of the ratchet limit due to the enhancement of the constraint effect. It is worth noting that although this linear relationship between the constraint parameter $\sqrt{A_p}$ and the ratchet limit is established by considering two extreme out-of-plane constraint states (i.e., the plane strain and plane stress states), for the actual 3D cracked structures, the data points should be on the correlation line. The correlation is very meaningful for the assessment of the ratchet limits of cracked structures in terms of different constraint conditions (including different in-plane, out-of-plane, and compound constraint conditions), where the constraint-related ratchet limit is able to be calculated through it directly.

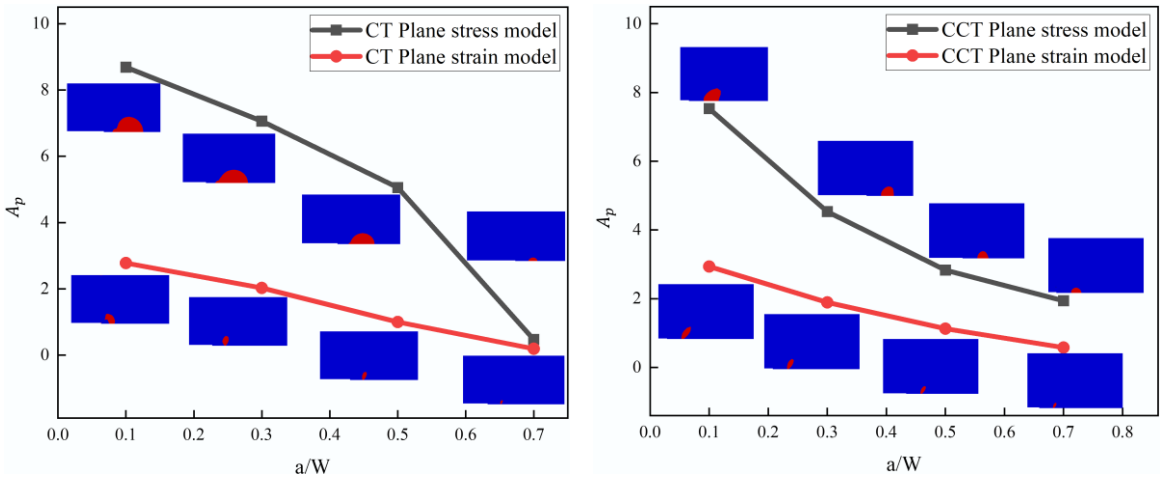

Fig. 12. The unified constraint effect measurement of cracked specimens under different constraint conditions for (a) CT specimen and (b) CCT specimen

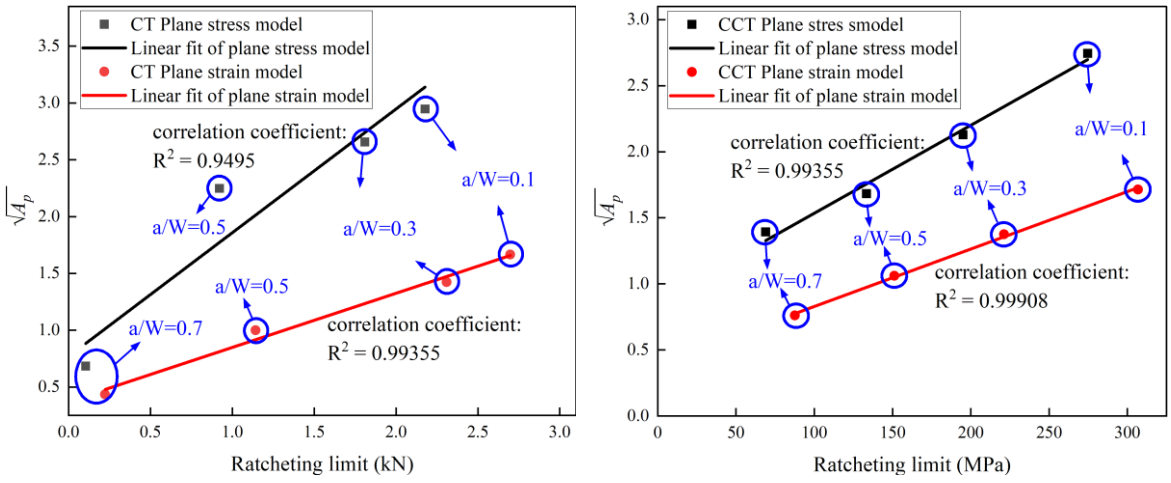

(a) (b)

Fig. 13. The general relationship between the unified constraint measurement $\sqrt{A_p}$ and the LMM ratchet limit under cyclic bending moment condition: (a) CT specimen and (b) CCT specimen

4.4. Effect of constraint on the plastic strain range and the unified correlation

Given that the structural low cycle fatigue failure and life are closely related to the amplitude of alternating plastic strain at the critical locations, it is meaningful to reveal the influence of the constraint effect in the cracked structure on the amplitude of alternating plastic strain. Therefore, based upon the DSCA procedure under the LMM framework introduced by Sections 2.2 and 2.4, two series of fatigue analyses for both CT and CCT specimens are implemented to acquire the convergent varying residual stress field and amplitude of alternating plastic strain range at the crack tip. Here, the load condition points are predefined to be lower than the values of the ratchet limit under both plane stress and plane strain conditions, which are displayed by the purple star points in Fig. 6 and Fig. 7, slightly falling into the reverse plastic zone of specimens with $a/W = 0.7$.

Regardless of the CT or CCT specimen, with the in-plane constraint gradually strengthening, the amplitude of the alternating strain at the crack tip has an apparent upward

trend, which is depicted by the two sets of closed stress-strain hysteretic curves in Fig. 14 and Fig. 15. Moreover, it is worth noting that there is a threshold of crack size at which the high constraint effect intervenes and intensively changes the cyclic strain range. For both specimens, when the a/W parameter is below 0.5, the increment of strain range for each size is almost uniform, while a surge of plastic strain range occurs with the crack parameter changing to 0.7 (see the green hysteresis loop in Fig. 14 and Fig. 15). However, the CCT specimen is not as sensitive to the constraint effect under the low in-plane constraint condition, which is reflected by the fact that when parameter a/W equals 0.1, and its cyclic strain range is still in a pure elastic state (see the short black dash curve in Fig. 15), resulting in much higher LCF life.

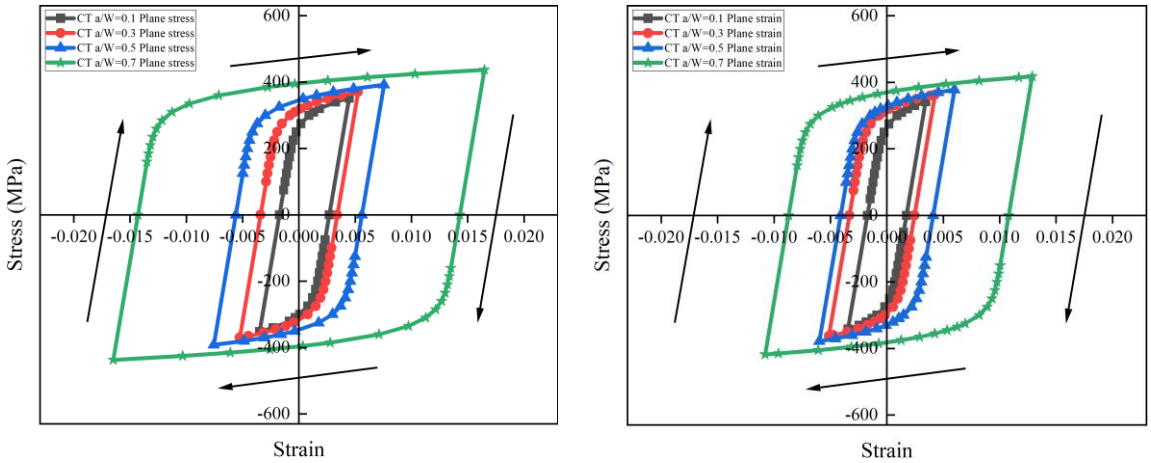

Fig. 14. Saturated hysteresis loops of CT specimen under reverse plasticity condition: (a) under plane stress condition and (b) under plane strain condition

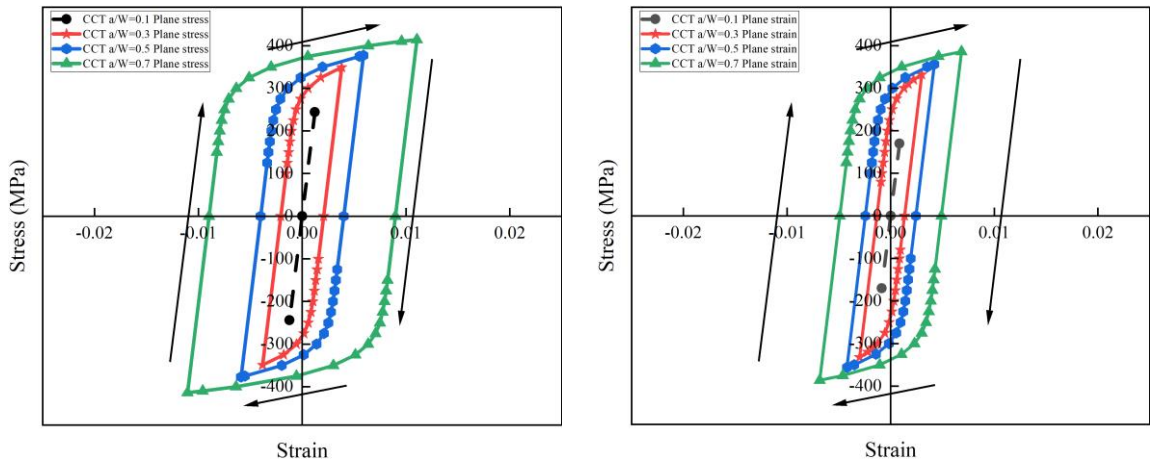

(a) (b)

Fig. 15. Saturated hysteresis loops of CCT specimen under reverse plasticity condition: (a) under plane stress condition and (b) under plane strain condition

The unified constraint parameter A_p is also adopted to further characterise the influence of the strength of constraint effect on the alternating plastic strain based on the DSCA results. There is a slight adjustment that since under the plastic shakedown load conditions, the local plastic region around the crack tip is not fully developed as in the ratcheting cases, the A_{PEEQ} to define the unified constraint parameter A_p is adjusted to the area surrounded by the alternating plastic strain isolines ahead of the crack tip. In this section, the alternating plastic strain range is selected to be 0.02 to determine the isolines ahead of the crack tip. In Fig. 16, there is a certain correlation between the unified constraint parameter $\sqrt{A_p}$ and the alternating plastic strain range at the crack tip, showing that as the compound constraint effect strengthens, the alternating plastic strain range increases linearly, which directly results in sharply reduced LCF life. Although there are only two extreme out-of-plane constraint states (i.e., the plane strain and plane stress states) exhibited here, the linear relationship line of specific 3D cracked structures should exist accordingly. This linear correlation is capable of functioning as the reduction coefficient for assessing the alternating plastic strain range and

the LCF life of cracked structures once the constraint effect strength is calibrated according to the parameter A_p.

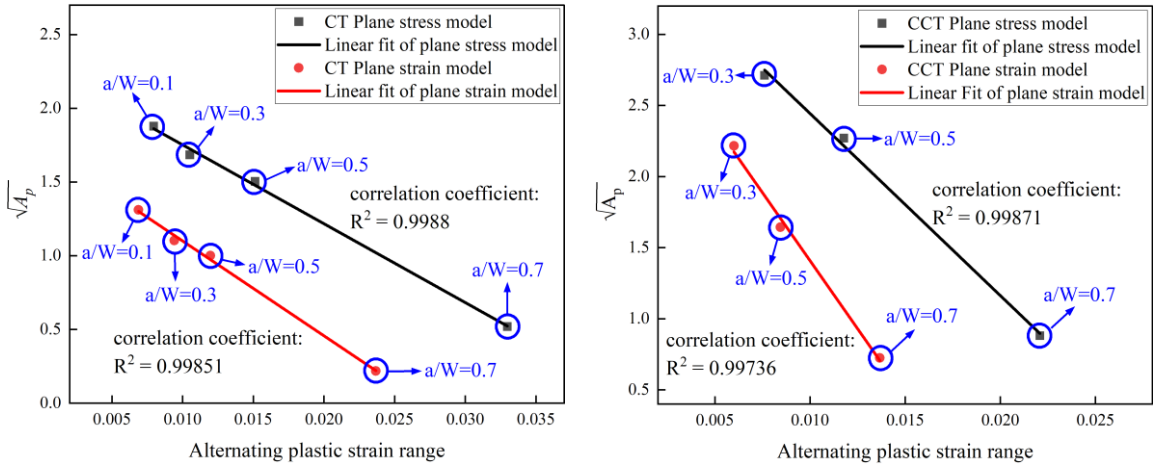

Fig. 16. The general relationship between the unified constraint measurement $\sqrt{A_p}$ and the alternating plastic strain under cyclic bending moment condition: (a) CT specimen and (b) CCT specimen

5. Verifications and discussions

5.1. Strategy of validation

The comparison of the numerical solutions with experimental data is always beneficial. However, in terms of this study, the experimental results are more suitable for verifying the trend and rule that dominate the failure mechanisms, since it is almost impossible for the numerical results to completely coincide with the results of real experiments due to many inevitable uncertain factors in the experiment process. Therefore, in this research, numerical verifications were implemented to verify the LMM ratcheting analysis which is applied in the virtual experiments when deriving the pertinent constraint parameter.

To verify the effectiveness of the ratcheting boundaries calculated by LMM ratcheting analysis, it is not necessary to verify all these ratcheting boundaries for all cases investigated, and we only need to verify the accuracy of ratcheting boundaries for some typical conditions. For this consideration, only the LMM ratcheting boundaries for both the CT specimen and CCT specimen with a/W=0.5 (Shown in Fig.17) were verified. Although the ratcheting boundaries will be different when using a different value for a/W as shown in Figs. 6 and 7, it will have no impact of using a different value for a/W on the validity of the verification process. This is because the Linear Matching Method is a general numerical approach, and the accuracy of the method does not rely on the geometry adopted. Two sets of virtual numerical tests are designed for both CT and CCT specimens by adopting the detailed ABAQUS non-linear analysis. The specimen whose crack size parameter a/W is equal to 0.5 is defined as the standard specimen and selected for validation purposes, with the same cyclic hardening material property (defined in Section 3.2) and BCs (illustrated by Fig. 3) adopted in the FEA model.

The multi-step FEA is implemented according to the load history in Fig. 5, where the maximum value of bending moment within the per load cycle and the constant value of the tensile load are determined by four pairs of condition points shown in the LMM ratcheting boundaries for standard CT and CCT specimens with $a/W = 0.5$ (see Fig. 17). The green and pink condition points inside the general ratcheting region represent the alternating plastic condition related to fatigue failure, while the blue and yellow points above the boundary prescribe the ratcheting condition (progressive plastic condition).

The criterion for verification is to witness a transition of dominated mechanism from the non-ratcheting to the ratcheting failure on both sides of the boundary. If the boundary is effective, there should exist a state of alternating plasticity with the load condition inside the boundary, and at the same time, under the load point outside the boundary, the ratcheting behaviour should be observed. To further decide the cyclic state during the load cycle

progresses, the accumulation of time-dependent effective plastic strain is extracted from the key node at the crack tip, which is defined by the ABAQUS variable plastic strain magnitude PEMAG [48] (PEMAG=$\sqrt{\frac{2}{3}\varepsilon^{pl}:\varepsilon^{pl}}$, where ε^{pl} characterizes the plastic strain tensor). And the history of PEMAG is able to identify whether there is a ratcheting or non-ratcheting state for structures under cyclic load conditions.

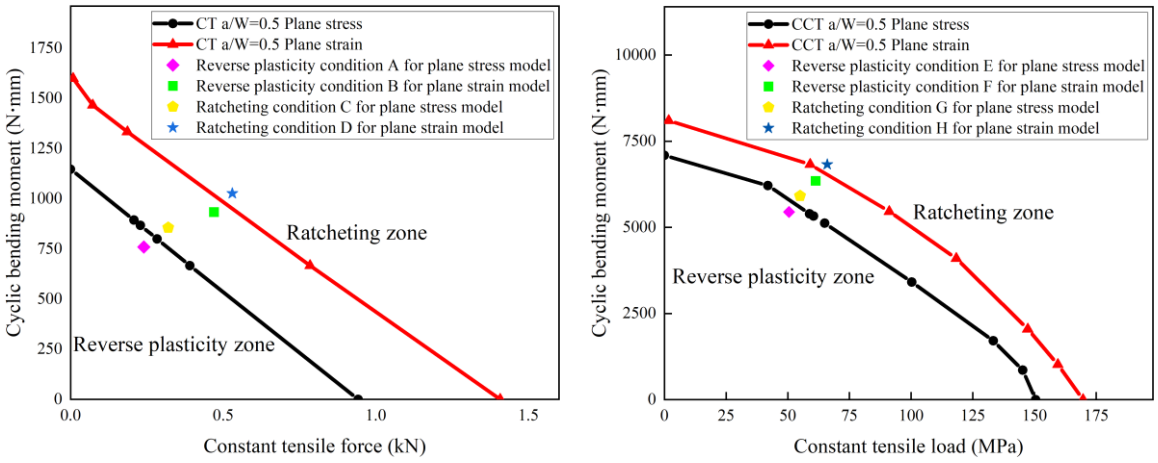

(a) (b)

Fig. 17. Load conditions for the verification of the LMM ratcheting boundaries: (a) Standard CT specimen (a/W=0.5) and (b) Standard CCT specimen (a/W=0.5)

5.2. Verification of CT specimen model

In the case of standard CT specimen, when the load combinations in Fig. 17 (a) are under the reverse plasticity condition, after the first load cycle (including loading and unloading processes), the plastic strain continues to fluctuate, and the amplitude finally converges to a fixed amplitude, which is displayed by the blue curves of plastic strain histories in Fig. 18. From another two blue curves in Fig. 19, it can be observed that with the crack tip entering the plastic shakedown state, except for the first cycle, all the subsequent

hysteresis loops always remain closed, and there is no net increment of plastic strain during this process.

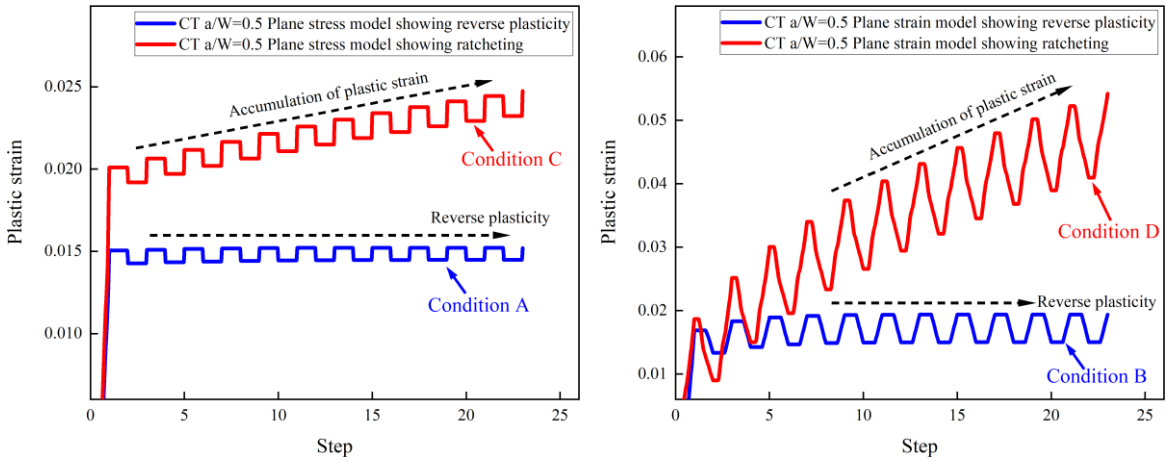

(a) (b)

Fig. 18. History of plastic strain magnitude at the crack tip: (a) standard CT specimen under plane stress condition and (b) standard CT specimen under plane strain condition

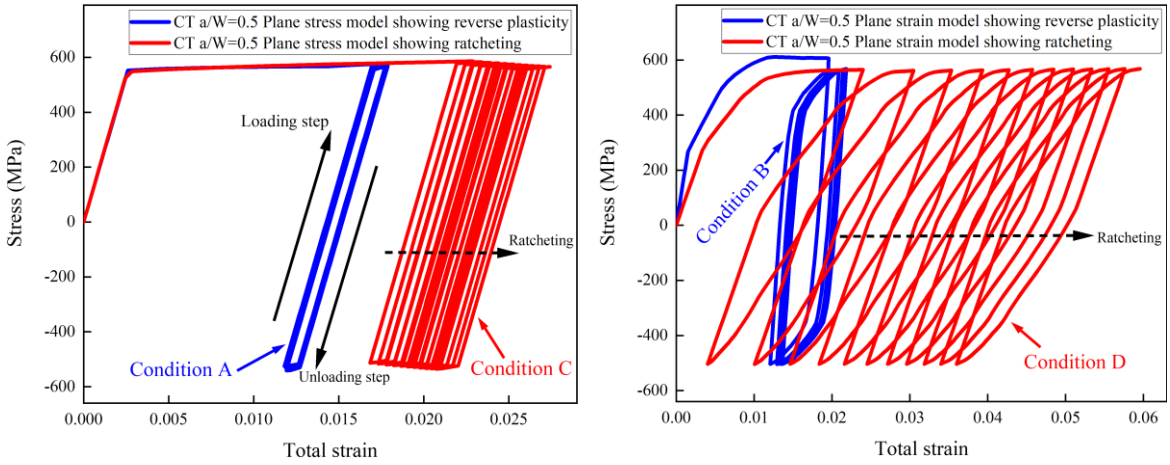

(a) (b)

Fig. 19. Cyclic stress-strain response at the crack tip: (a) standard CT specimen under plane stress condition and (b) standard CT specimen under plane strain condition

Instead, after the load condition points slightly rise to the ratcheting side, the net increase in cyclic plastic strain begins to occur, and it accumulates unstoppably during each cycle until progressive plastic collapse occurs. This process is described by the plastic strain history and stress-strain hysteresis curves shown in Fig. 18 (b) and Fig. 19 (b). Compared with the alternating plastic behaviour, the materials yield zone where progressive plastic strain occurs extends to a much broader range than the case of reverse plasticity condition, which is highly consistent with the failure mechanisms predicted by LMM ratcheting analysis.

5.3. Verification of CCT specimen model

To further explain the alternating plasticity at the crack tip of standard CCT specimen when the load condition points fall into the reverse plasticity zone in Fig. 17 (b), by tracking the historical information of stress and strain at the crack tip, a series of converged cyclic plastic strain ranges and closed hysteresis loops can be observed clearly from the blue curves in Fig. 20 and Fig. 21. In addition, similar to the phenomenon of the CT specimen above, the plastic yield zone, as well as the cyclic plastic strain response, are generated only near the crack tip

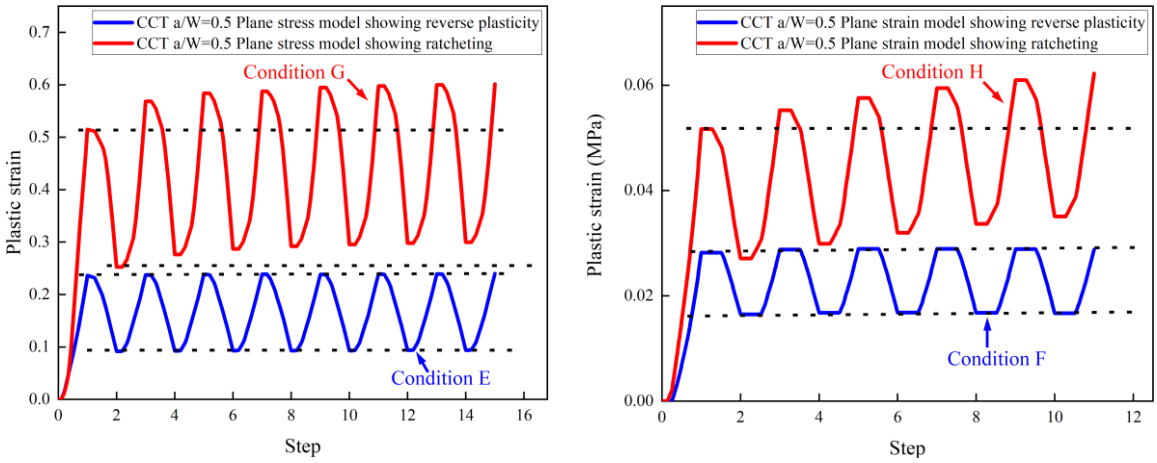

(a) (b)

Fig. 20. History of plastic strain magnitude at the crack tip: (a) standard CCT specimen under plane stress condition and (b) standard CCT specimen under plane strain condition

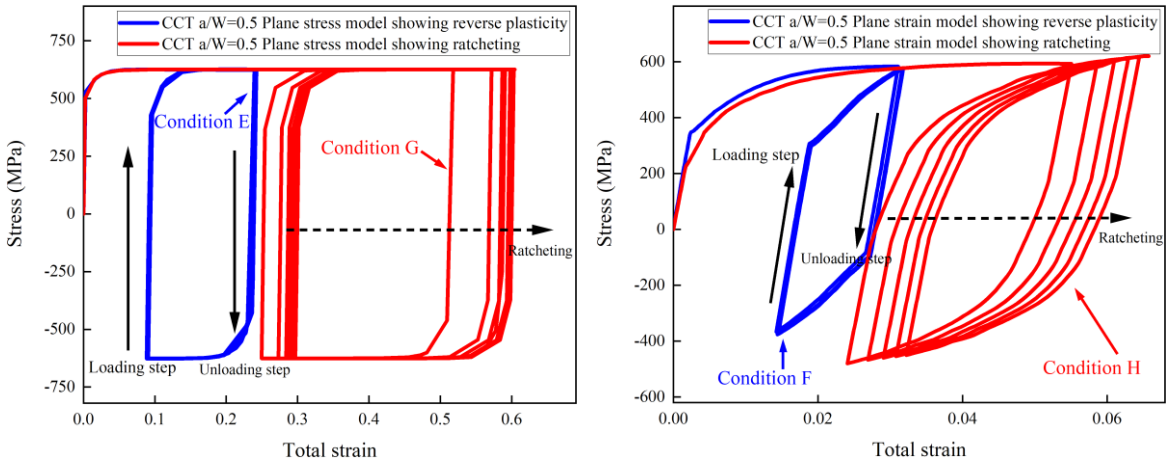

(a) (b)

Fig. 21. Cyclic stress-strain response at the crack tip: (a) standard CCT specimen under plane stress condition and (b) standard CCT specimen under plane strain condition

Compared to the standard CT case, the ratcheting strain at the standard CCT specimen crack tip develops more slowly when the load combinations lie slightly outside the ratcheting boundary, which is reflected by the red ratcheting curves in Fig. 20 and Fig. 21, where the increment of cyclic plastic strain during every cycle accumulates gradually at a low speed. This fact also provides sufficient evidence for the above prediction of failure mode determined by the LMM ratcheting analysis.

6. Conclusions

In this research, with the constraint effect involved, cyclic plastic responses of the cracked structure are investigated by using the direct method. The constraint-related ratcheting boundary of the cracked specimen is well-built, and the influence of the constraint

effect on the ratcheting boundary is clarified. In addition, the fracture mechanics constraint parameter Ap is generalized to measure the constraint-related alternating plasticity and ratcheting resistance.

The main conclusions of this study are as follows:

(1) The high in-plane constraint effect keeps compressing the capacity of both CT and CCT specimens against ratcheting failure due to cyclic load conditions as the in-plane constraint increases. With regard to the out-of-plane constraint effect, the acceptable plastic shakedown regions in the plane strain model are larger than in the plane stress model since the out-of-plane constraint effect elevates the resistance of ratcheting failure.

(2) The ratcheting boundary of the cracked specimen is much more vulnerable under the influence of the high in-plane constraint effect. And there is a significant nonlinear relationship between the weakening of the structural capacity against cyclic load conditions and the strengthening of in-plane constraint.

(3) The unified constraint parameter A_p is employed to measure the strength of compound constraint under cyclic loading conditions, showing that this unified constraint parameter is suitable for both monotonic and cyclic loading conditions. And a salient linear relation between parameter $\sqrt{A_p}$ and cyclic plastic responses (including ratchet limit and alternating plasticity) of the cracked specimen is demonstrated, aiming at evaluating the ratchet limits and alternating plastic strain range (associated with LCF life) of cracked structures in terms of different constraint conditions.

(4) As the load condition point falls into the reverse plasticity zone, there is a threshold of crack dimension at which the high constrain effect intervenes and intensively expands the amplitude of alternating plastic strain around the crack tip, leading to a sharp reduction in low cycle fatigue life.

(5) The ratcheting and alternating plasticity behaviours of standard CT and CCT specimens, predicted by the LMM framework, are verified by a detailed ABAQUS step-by-step analysis. The load condition points located at both sides of the ratcheting boundary show different failure mechanisms, which are completely consistent with those obtained by LMM ratcheting analysis.

Acknowledgements

This project is supported by National Natural Science Foundation of China (Grant No. 52150710540, 51975378 and 51828501) and Shanghai foreign experts project (Grant No. 21WZ2503200). The authors also would like to thank University of Shanghai for Science and Technology, East China University of Science and Technology, University of Strathclyde and Shanghai Municipal Education Commission for their support.

REFERENCES

[1] W. Brocks, W. Schmitt, The second parameter in J-R curves: constraint or triaxiality?, Constraint Effects in Fracture Theory and Applicatons: Second Volume, ASTM International1995.
[2] S.-G. Larsson, A.J. Carlsson, Influence of non-singular stress terms and specimen geometry on small-scale yielding at crack tips in elastic-plastic materials, Journal of the Mechanics and Physics of Solids 21(4) (1973) 263-277.
[3] N.P. O'Dowd, C.F. Shih, Family of crack-tip fields characterized by a triaxiality parameter—II. Fracture applications, Journal of the Mechanics and Physics of Solids 40(5) (1992) 939-963.
[4] N. O'dowd, C.F. Shih, Family of crack-tip fields characterized by a triaxiality parameter—I. Structure of fields, Journal of the Mechanics and Physics of Solids 39(8) (1991) 989-1015.
[5] Y. Chao, S. Yang, M. Sutton, On the fracture of solids characterized by one or two parameters: theory and practice, Journal of the Mechanics and Physics of Solids 42(4) (1994) 629-647.
[6] G. Wanlin, Elasto-plastic three-dimensional crack border field—III. Fracture parameters, Engineering Fracture Mechanics 51(1) (1995) 51-71.
[7] W. Guo, Elastoplastic three dimensional crack border field—II. Asymptotic solution for the field, Engineering Fracture Mechanics 46(1) (1993) 105-113.
[8] W. Guo, Elastoplastic three dimensional crack border field—I. Singular structure of the field, Engineering Fracture Mechanics 46(1) (1993) 93-104.
[9] M. Mostafavi Majd, M. Pavier, D. Smith, Unified measure of constraint, International Conference on Engineering Structural Integrity Assessment, Manchester, 2009.
[10] M. Mostafavi, D. Smith, M. Pavier, Fracture of aluminium alloy 2024 under biaxial and triaxial loading, Engineering fracture mechanics 78(8) (2011) 1705-1716.
[11] M. Mostafavi, D. Smith, M. Pavier, A micromechanical fracture criterion accounting for in-plane and out-of-plane constraint, Computational materials science 50(10) (2011) 2759-2770.
[12] M. Mostafavi, D. Smith, M. Pavier, Reduction of measured toughness due to out‐of‐plane constraint in ductile fracture of aluminium alloy specimens, Fatigue & Fracture of Engineering Materials & Structures 33(11) (2010) 724-739.
[13] J. Yang, G. Wang, F. Xuan, S. Tu, Unified correlation of in-plane and out-of-plane constraint with fracture resistance of a dissimilar metal welded joint, Engineering Fracture Mechanics 115 (2014) 296-307.
[14] J. Yang, G. Wang, F. Xuan, S. Tu, Unified correlation of in‐plane and out‐of‐plane constraints with fracture toughness, Fatigue & Fracture of Engineering Materials & Structures 37(2) (2014) 132-145.
[15] J. Yang, G. Wang, F. Xuan, S. Tu, Unified characterisation of in‐plane and out‐of‐plane constraint based on crack‐tip equivalent plastic strain, Fatigue & Fracture of Engineering Materials & Structures 36(6) (2013) 504-514.
[16] J.Y. Xu, G.Z. Wang, F.Z. Xuan, S.T. Tu, Unified constraint parameter based on crack-tip opening displacement, Engineering Fracture Mechanics 200 (2018) 175-188.
[17] D. Wu, H. Jing, L. Xu, L. Zhao, Y. Han, Analytical approaches of creep crack initiation prediction coupled with the residual stress and constraint effect, European Journal of Mechanics - A/Solids 71 (2018) 1-15.
[18] D. Wu, H. Jing, L. Xu, L. Zhao, Y. Han, Enhanced models of creep crack initiation prediction coupled the stress-regime creep properties and constraint effect, European Journal of Mechanics - A/Solids 74 (2019) 145-159.

[19] D. Wu, H. Jing, L. Xu, Engineering application of enhanced C*-Q* two parameter approaches for predicting creep crack initiation times, European Journal of Mechanics - A/Solids 82 (2020) 104013.
[20] H. Chen, W. Chen, J. Ure, A Direct Method on the Evaluation of Cyclic Steady State of Structures With Creep Effect, Journal of Pressure Vessel Technology 136(6) (2014).
[21] T. Li, H. Chen, W. Chen, J. Ure, On the Ratchet Analysis of a Cracked Welded Pipe, Journal of Pressure Vessel Technology 134(1) (2011).
[22] H. Chen, W. Chen, T. Li, J. Ure, Effect of circular holes on the ratchet limit and crack tip plastic strain range in a centre cracked plate, Engineering fracture mechanics 78(11) (2011) 2310-2324.
[23] K.B. Cochran, R.H. Dodds, K.D. Hjelmstad, The role of strain ratcheting and mesh refinement in finite element analyses of plasticity induced crack closure, Int J Fatigue 33(9) (2011) 1205-1220.
[24] S.K. Paul, S. Tarafder, Cyclic plastic deformation response at fatigue crack tips, International Journal of Pressure Vessels and Piping 101 (2013) 81-90.
[25] T.B. Li, H.F. Chen, W.H. Chen, J. Ure, On the Ratchet Analysis of a Cracked Welded Pipe, J Press Vess-T Asme 134(1) (2012).
[26] J. Tong, C. Cornet, B. Lin, C. Lupton, H.Y. Li, P. Bowen, S. Williams, M. Hardy, Near-tip strain ratchetting and crack growth at elevated temperature, Int J Fatigue 82 (2016) 514-520.
[27] A. Bahloul, C. Bouraoui, The overload effect on the crack-tip cyclic plastic deformation response in SA333 Gr 6 C-Mn steel, Theoretical and Applied Fracture Mechanics 99 (2019) 27-35.
[28] S.K. Paul, Numerical models of plastic zones and associated deformations for a stationary crack in a C(T) specimen loaded at different R-ratios, Theoretical and Applied Fracture Mechanics 84 (2016) 183-191.
[29] B.S. Report, SINTAP. Structural assessment procedures for European industry, final procedure, project BE95-1426, Rotherham, 1999.
[30] B.E. Ltd, R6: Assessment of the integrity of structures containing defects, British energy generation report R/H/R6, revision 4, Gloucester, UK, 2007.
[31] M. Koçak, Webster, S., Janosch, J.J., Ainsworth, R.A., Koers, R., FITNET Fitness-for-Service (FFS) - Procedure (Volume 1), printed by GKSS Research Center, Geesthacht, Germany, 2008.
[32] M. Koçak, Hadley, I., Szavai, S., Tkach, Y., Taylor, N., FITNET Fitness-for-Service (FFS) - Annex (Volume 2), printed by GKSS Research Center, Geesthacht, Germany, 2008.
[33] B. Wang, T. Siegmund, Numerical simulation of constraint effects in fatigue crack growth, Int J Fatigue 27(10) (2005) 1328-1334.
[34] V.B. Pandey, S.S. Samant, I.V. Singh, B.K. Mishra, An improved methodology based on continuum damage mechanics and stress triaxiality to capture the constraint effect during fatigue crack propagation, Int J Fatigue 140 (2020) 105823.
[35] H. Shen, W. Guo, 3D constraint effect on 3D fatigue crack propagation, Int J Fatigue 27(6) (2005) 617-623.
[36] J. Yang, Y. Liu, H. Chen, A study on the matching of constraint between steam turbine blade and laboratory specimens, Advances in Mechanical Engineering 12(5) (2020) 1687814020922007.
[37] J.P. Tan, G.Z. Wang, F.Z. Xuan, S.T. Tu, Correlation of creep crack-tip constraint between axially cracked pipelines and test specimens, International Journal of Pressure Vessels and Piping 98 (2012) 16-25.
[38] H.F. Chen, A.R.S. Ponter, A method for the evaluation of a ratchet limit and the amplitude of plastic strain for bodies subjected to cyclic loading, Eur J Mech a-Solid 20(4) (2001) 555-571.
[39] H.F. Chen, A.R.S. Ponter, A Direct Method on the Evaluation of Ratchet Limit, J Press Vess-T Asme

132(4) (2010).
[40] H.F. Chen, A.R.S. Ponter, Shakedown and limit analyses for 3-D structures using the linear matching method, International Journal of Pressure Vessels and Piping 78(6) (2001) 443-451.
[41] Z. Liu, X. Wang, S. Shi, Y. Shen, X. Chen, Application of modified normalization method for JR curve determination using clamped SENT specimens with varying in-plane and out-of-plane constraints, Engineering Fracture Mechanics (2020) 106968.
[42] Z. Liu, X. Wang, R.E. Miller, J. Hu, X. Chen, Ductile fracture properties of 16MND5 bainitic forging steel under different in-plane and out-of-plane constraint conditions: Experiments and predictions, Engineering Fracture Mechanics (2020) 107359.
[43] X.Q. Wu, Y. Katada, Strain-amplitude dependent fatigue resistance of low-alloy pressure vessel steels in high-temperature water, Journal of Materials Science 40(8) (2005) 1953-1958.
[44] ASTM, ASTM A508 / A508M-18, Standard Specification for Quenched and Tempered Vacuum-Treated Carbon and Alloy Steel Forgings for Pressure Vessels, West Conshohocken, PA, 2018.
[45] R. Beesley, H. Chen, M. Hughes, A novel simulation for the design of a low cycle fatigue experimental testing programme, Comput Struct 178 (2017) 105-118.
[46] ASME, ASME Boiler & Pressure Vessel Code, Section VIII Rules for Construction of Pressure Vessels Division 2, Alternative Rules, The American Society of Mechanical Engineers, New York, 2015.
[47] ASME, ASME Boiler & Pressure Vessel Code, Section II Materials Part D, Properties (Metric), The American Society of Mechanical Engineers, New York, 2015.
[48] D. Systèmes, Abaqus 6.12 Abaqus User's Manual, USA, 2012.
[49] ASTM E1820-08a. Standard test method for measurement of fracture toughness, American Society for Testing and Materials, Philadelphia, 2008.
[50] H.S. Ma, G.Z. Wang, S. Liu, S.T. Tu, F.Z. Xuan, Three-dimensional analyses of unified characterization parameter of in-plane and out-of-plane creep constraint, Fatigue & Fracture of Engineering Materials & Structures 39(2) (2016) 251-263.
[51] H.T. Wang, G.Z. Wang, F.Z. Xuan, S.T. Tu, Numerical investigation of ductile crack growth behavior in a dissimilar metal welded joint, Nucl Eng Des 241(8) (2011) 3234-3243.